Journal of Solid State Chemistry **155,** 168–176 (2000)
doi:10.1006/jssc.2000.8931, available online at http://www.idealibrary.com on IDEAL®

Synthesis, Structure, and Properties of $Eu_{16}Sb_{11}$ and $Eu_{16}Bi_{11}$

Julia Y. Chan,[1] Marilyn M. Olmstead, Håkon Hope, and Susan M. Kauzlarich[2]

Department of Chemistry, One Shields Avenue, University of California, Davis, California 95616

Received May 30, 2000; in revised form August 1, 2000; accepted August 15, 2000

DEDICATED TO PROFESSOR J. M. HONIG

The compounds $Eu_{16}Sb_{11}$ and $Eu_{16}Bi_{11}$ have been prepared from the elements in Ta containers by heating at 1100°C and then slowly cooled to 1000°C over 4 days.These compounds are isostructural with the Zintl-phase $Ca_{16}Sb_{11}$ and crystallize in the tetragonal space group $P\bar{4}2_1m$ ($Z = 2$). The structures were determined from single-crystal X-ray data ($T = 143$ K) for $Eu_{16}Sb_{11}$ ($a = 12.674$ (2) Å, $c = 11.720$ (2) Å, $R_1 = 4.04\%$ $wR2 = 10.84\%$), and $Eu_{16}Bi_{11}$ ($a = 12.885$ (2) Å, $c = 11.883$ (4) Å, $R_1 = 6.09\%$, $wR2 = 15.24\%$). The $Ca_{16}Sb_{11}$ structure type can be described as pairs of face-shared square antiprisms that are joined by means of a square prism to form a columnar chain composed of Ca^{2+} cations and centered by Sb anions along the *c* axis. The columns are associated by means of Ca–Ca bonds that alternate long and short along the *c* axis in a ladder-like fashion. Along the *a* and *b* axes, there is an intergrowth of square prism, antiprism columns alternating with columns of face-sharing hexagonal antiprisms. The structures of these Eu compounds are compared with those of $Ca_{16}Sb_{11}$. Temperature-dependent resistivity of $Eu_{16}Sb_{11}$ indicates that it is a semiconductor. Magnetization measurements show that $Eu_{16}Sb_{11}$ and $Eu_{16}Bi_{11}$ are paramagnetic. The effective moment in the paramagnetic state for $Eu_{16}Sb_{11}$ is $\mu_{exp} = 32.2$ (1) μ_B per formula unit (8.06 (3) μ_B/Eu atom) and for $Eu_{16}Bi_{11}$, $\mu_{exp} = 33.6$ (2) μ_B/formula unit (8.40 (6) μ_B/Eu atom), consistent with divalent Eu^{2+} cations ($\mu_{eff} = 7.94$ μ_B/Eu atom).

INTRODUCTION

The incorporation of rare-earth elements into known structure types provides a means to alter the magnetic and electronic properties in the design of new materials. The *RE*–*Pn* (*RE* = rare earth; *Pn* = As, Sb, Bi) systems have been extensively investigated due to their magnetic and electronic properties (1). The various phases include RE_5Pn_3 (2), RE_4Pn_3 (3), and $RE_{11}Pn_{10}$ (4, 5). Some of the rare earth pnictides show anomalous magnetic and electronic behavior (6). These include mixed antiferromagnetism for Ce*Pn* (*Pn* = As, Sb, Bi), metamagnetism for Nd*Pn*, and antiferromagnetism for Gd, Tb, Dy, Ho, and Er monopnictides. In the anti-Th_3P_4 or Gd_4Bi_3 structure type (7), properties range from superconducting for La_4As_3, to antiferromagnetic for Eu_3GdSb_3 and Eu_4Bi_3 (3), and to ferromagnetic for RE_4Sb_3 (*RE* = Pr, Nd, Sm, Yb, and other mixed rare earths) (8). Other compounds with divalent Eu cations include EuAs, EuP_2, Eu_5As_4, Eu_2As_3, Eu_3As_4, EuP_3, EuP_7 (8), and $Eu_{11}Sb_{10}$, which appears to be antiferromagnetic below $T_N \approx 5$ K (5).

The results of an extended study of compounds of the $Ca_{16}Sb_{11}$ structure type were recently reported (9). This structure type was compared to the $Ho_{11}Ge_{10}$ (10) and Ca_5Sb_3 (11) phases. The possible role of hydrogen in this apparently electron imprecise system was discussed and discarded. A distinct characteristic of the $Ca_{16}Sb_{11}$ structure is the 50 : 50 splitting of an Sb site, which appears to result from the surplus space in the square prismatic cavity afforded by Ca. There are no interstitials, but rather the structure can be described as $[16Ca^{2+} + 10Sb^{3-} + \frac{1}{2}Sb_2^{4-}]$ and, accordingly, is valence precise. An elongated displacement ellipsoid for one of the Sb's provides support for the hypothesis of an Sb_2^{4-} anion that is suggested to occur in a spatially disordered manner in the structure. The fact that all the alkaline earth analogs are diamagnetic semiconductors supports the hypothesis of charge localization. The lattice parameters of $Eu_{16}Sb_{11}$ and $Eu_{16}Bi_{11}$ were reported; however, the single-crystal structures were not determined and the magnetic properties were not reported. This paper describes the synthesis, structure, and magnetic properties of $Eu_{16}Sb_{11}$ and $Eu_{16}Bi_{11}$.

EXPERIMENTAL

Synthesis

Eu metal was obtained from Ames Laboratory and cut into small pieces. Sb shot (J. Matthey, 99.99%) was used as received. Bi needles (Anderson Physics, 99.999%) were ground into powder. All materials were handled in an

[1] Current address: Department of Chemistry, 232 Choppin Hall, Louisiana State University, Baton Rouge, LA 70803-1804.

[2] To whom correspondence should be addressed.

0022-4596/00 $35.00

argon-filled drybox. The datum crystal of $Eu_{16}Sb_{11}$ was obtained via a reaction designed to produce Eu_8MnSb_5. Subsequently, the stoichiometric reaction was optimized and the Bi phase was also prepared. All of the $Eu_{16}Sb_{11}$ and $Eu_{16}Bi_{11}$ samples were prepared by weighing stoichiometric amounts of the elements in a drybox and loading into a clean tantalum tube with a sealed end. Ta tubes had been cleaned prior to arc welding with 20% HF, 25% HNO_3, and 55% H_2SO_4 solution. The tube was crimp shut, transferred to an argon-filled arc welder, and sealed. The sealed Ta tube was further sealed in a fused silica tube under $\frac{1}{5}$ atm purified argon. Quantitative yields of reflective polycrystalline pieces and platelike single crystals of $Eu_{16}Pn_{11}$ were obtained by heating the mixtures at 30°C/h to 1100°C for 1 day and cooling to 1000′C and then to room temperature at 30°C/h. All reaction tubes were opened and examined in a nitrogen-filled drybox equipped with a microscope. These rare earth compounds do not appear to be air sensitive; powder diffraction patterns of the compounds exposed to air were identical to those of samples that had been handled in the drybox.

X-Ray Powder Diffraction

The products were examined in a drybox under an atmosphere of N_2, ground up with a mortar and pestle, mixed with approximately 10% silicon, and placed between two pieces of cellophane tape. The sample was transferred to an Enraf Nonius Guinier camera utilizing Cu$K\alpha_1$ radiation. Powder diffraction patterns were compared to those calculated from crystal structure data using the program POWDER (12). Diffraction line positions were read and 2θ values, d spacings, and standard deviations were obtained from the program GUIN (13). Diffraction lines were indexed and the lattice parameters refined using the program LATT (14).

Single-Crystal X-Ray Diffraction

The tantalum tube was opened in a drybox equipped with a microscope. A set of potential crystals for single-crystal structure determination were transferred to Exxon Paratone N oil. A suitable crystal was mounted on a thin glass fiber and positioned in a cold stream of N_2 on an R3m/V Siemens diffractometer with a modified Enraf–Nonius low-temperature apparatus (Mo$K\alpha$, $\lambda = 0.71073$ Å), and a graphite monochromator. Data collection parameters and crystallographic data are provided in Table 1. The lattice parameters were verified from axial photographs. Long-exposure axial photos were also examined to verify that compounds of this structure type have no detectable superstructure or alternate cell. No decomposition of the crystal was observed during data collection (inferred from the intensity of two check reflections). Emperical absorption corrections were applied to the data sets: a ψ-scan correction for $Eu_{16}Sb_{11}$ and XABS2 (15) for $Eu_{16}Bi_{11}$. The structures were refined using SHELXTL-97 (16). Problems similar to those described for $Ca_{16}Sb_{11}$ (9) were encountered. The $Pn(1)$ position was best modeled as a split position with 50% occupancy required by symmetry. A number of other space groups were examined, however; the only satisfactory refinement was achieved in the noncentrosymmetric space group $P\bar{4}2_1m$. The structures were refined as racemic twins. The absorption by $Eu_{16}Bi_{11}$ contributed to additional problems with refinement, reflected in the large final $R1$ and $wR2$ values. Atomic coordinates and isotropic thermal parameters are provided in Table 2. Anisotropic thermal parameters for each structure are provided in Table 3.

TABLE 1
Crystallographic Daata for $Eu_{16}Sb_{11}$ and $Eu_{16}Bi_{11}$ ($P\bar{4}2_1m$, $Z = 2$)

	$Eu_{16}Sb_{11}$	$Eu_{16}Bi_{11}$
Crystal dimension (mm)	$0.08 \times 0.12 \times 0.20$	$0.02 \times 0.06 \times 0.1$
Lattice parameters (Å)	$a = 12.674(2)$	$a = 12.885(1)$
(143 K)	$c = 11.720(2)$	$c = 11.83(3)$
Cell volume (Å^3)	$V = 1882.6(5)$	$V = 1972.9(1)$
2θ max	55°	55°
No. of collected reflections	2312	4734
No. of unique reflections	2312	2404 [R(int) = 0.11]
No. of parameters refined	78	78
ρ_{cal} (Mg m^{-3})	6.652	7.963
μ Mo$K\alpha$ (mm^{-1})	33.91	73.82
$R1^a$ (data with $F_o > 4\sigma(F_o)$)	0.0404	0.0609
$wR2^b$ (all data)	0.1084	0.152
Largest diff. peak and hole (eA^{-3})	2.01 and −2.44	4.1 and −3.2

$^a R = \sum||F_o| - |F_c||/\sum|F_o|$
$^b wR^2 = \sum[w(F_o^2 - F_c^2)^2]/\sum[w(F_o^2)^2]^{\frac{1}{2}}$

Magnetic Susceptibility Measurements

Magnetization data were obtained with a Quantum Design MPMS Superconducting Quantum Interference Device (SQUID) magnetometer with a 5.5-T superconducting magnet. The data were collected and analyzed with the Magnetic Property Measurement System (MPMS) software supplied by Quantum Design (17). The samples were prepared in a drybox by loading 20 to 25 mg of powdered sample into a quartz tube designed to provide a uniform background. The tube was subsequently sealed under vaccum (1×10^{-6} Torr). The temperature-dependent magnetization data were obtained by first measuring the zero-field-cooled (ZFC) magnetization in the field while warming from 5 to 300 K and then measuring magnetization while cooling back to 5 K with the field applied to obtain the field-cooled (FC) data.

TABLE 2

Atomic Coordinates ($\times 10^4$) and Equivalent Isotropic Displacement Parameters ($Å^2 \times 10^3$) (U(eq) Is Defined as One-Third of the Trace of the Orthogonalized U_{ij} Tensor)

	$Eu_{16}Sb_{11}$			
	x	y	z	U(eq)
Sb(1)[a]	0	0	4716(2)	29(1)
Sb(2)	0	0	1450(2)	36(1)
Sb(3)	3750(1)	8750(1)	4892(2)	28(1)
Sb(4)	3560(1)	8560(1)	290(2)	30(1)
Sb(5)	1795(1)	6795(1)	7613(1)	25(1)
Sb(6)	1675(1)	6675(1)	2360(1)	24(1)
Eu(1)	0	5000	7902(2)	28(1)
Eu(2)	0	5000	1496(2)	32(1)
Eu(3)	1334(1)	6334(1)	4998(1)	28(1)
Eu(4)	2913(1)	5897(1)	− 15(1)	28(1)
Eu(5)	4254(1)	7088(1)	2897(1)	28(1)
Eu(6)	693(1)	2029(1)	3132(1)	37(1)
	$Eu_{16}Bi_{11}$			
	x	y	z	U(eq)
Bi(1)[a,b]	0	0	4823(3)	25(1)
Bi(2)	0	0	1504(1)	18(1)
Bi(3)	3766(1)	8766(1)	4937(2)	20(1)
Bi(4)	3553(1)	8553(1)	183(2)	26(1)
Bi(5)	1776(1)	6776(1)	7631(2)	15(1)
Bi(6)	1705(1)	6705(1)	2360(2)	16(1)
Eu(1)	0	5000	7996(4)	24(1)
Eu(2)	0	5000	1624(4)	28(1)
Eu(3)	1353(1)	6352(1)	5000(3)	23(1)
Eu(4)	2919(1)	5882(1)	− 8(2)	16(1)
Eu(5)	4267(2)	7088(2)	2953(2)	22(1)
Eu(6)	700(2)	2055(2)	3081(2)	26(1)

[a] 50% occupancy.
[b] Refined isotropically.

Field-dependent magnetization data were taken at 5 K with H swept from 5 to − 5 T and back.

Resistivity Measurements

Temperature-dependent resistivity measurements were performed on elongated polycrystalline pieces of $Eu_{16}Sb_{11}$ obtained in the reaction product. Four stainless steel wires placed in-line were held onto the sample by pressure. The sample was placed into a closed-cycle refrigerator. Ohm's law was verified at room temperature. A Keithley Model 224 current source and a Keithley Model 182 nanovoltmeter were used to measure resistivity. Below 250 K, the resistance became too high to measure. Thermal voltages were minimized by reversal of current bias. Temperature dependence of the data indicated semiconducting behavior for $Eu_{16}Sb_{11}$.

RESULTS AND DISCUSSION

Structure

Crystal data and data collection parameters for $Eu_{16}Sb_{11}$ and $Eu_{16}Bi_{11}$ are provided in Table 1. Coordination distances to each atom in the asymmetric unit are provided in Table 4 for both the Sb and Bi compounds. The structure was solved by direct methods and found to be isostructural with $Ca_{16}Sb_{11}$ (9). It was solved and refined in the tetragonal space group $P\bar{4}2_1m$. The room temperature lattice parameters obtained from powder X-ray data of $Eu_{16}Sb_{11}$ are $a = 12.689$ (1) Å and $c = 11.721$ (2) Å. Compared to the values given by Leon-Escamilla *et al.* (9), this a axis is 0.05 Å shorter and the c axis 0.05 Å longer. The room temperature lattice parameters for the Bi sample ($a = 12.910$ (3) Å and $c = 11.856$ (4) Å) are, within standard deviations, the same as the values previously published (9).

The asymetric unit consists of 4 Eu atoms and 2.75 Sb atoms in the asymmetric unit. The structure can be

TABLE 3

Anisotropic Displacement Parameters ($Å^2 \times 10^3$) for $Eu_{16}Sb_{11}$ and $Eu_{16}Bi_{11}$ (The Anisotropic Displacement Factor Exponent Takes the Form $-2\pi^2(h^2a^{*2}U^{11} + \cdots + 2hka^*b^*U^{12})$)

	$Eu_{16}Sb_{11}$					
	U^{11}	U^{22}	U^{33}	U^{23}	U^{13}	U^{12}
Sb(1)	29(2)	36(2)	24(2)	0	0	4(2)
Sb(2)	24(1)	24(1)	60(1)	0	0	1(1)
Sb(3)	29(1)	29(1)	27(1)	− 1(1)	− 1(1)	4(1)
Sb(4)	26(1)	26(1)	40(1)	0(1)	0(1)	− 1(1)
Sb(5)	28(1)	28(1)	20(1)	0(1)	0(1)	0(1)
Sb(6)	26(1)	26(1)	19(1)	0(1)	0(1)	− 1(1)
Eu(1)	26(1)	26(1)	33(1)	0	0	0(1)
Eu(2)	29(1)	29(1)	38(1)	0	0	− 3(1)
Eu(3)	33(1)	33(1)	20(1)	− 1(1)	− 1(1)	1(1)
Eu(4)	34(1)	30(1)	21(1)	0(1)	1(1)	− 1(1)
Eu(5)	27(1)	28(1)	28(1)	− 4(1)	1(1)	0(1)
Eu(6)	26(1)	36(1)	48(1)	− 17(1)	− 5(1)	3(1)
	$Eu_{16}Bi_{11}$					
	U^{11}	U^{22}	U^{33}	U^{23}	U^{13}	U^{12}
Bi(2)	13(1)	14(1)	27(1)	0	0	0(1)
Bi(3)	22(1)	22(1)	16(1)	0(1)	0(1)	5(1)
Bi(4)	15(1)	15(1)	46(2)	0(1)	0(1)	0(1)
Bi(5)	16(1)	16(1)	12(1)	− 1(1)	− 1(1)	1(1)
Bi(6)	17(1)	17(1)	12(1)	0(1)	0(1)	− 1(1)
Eu(1)	16(1)	16(1)	41(2)	0	0	0(2)
Eu(2)	16(1)	16(1)	51(3)	0	0	− 6(2)
Eu(3)	29(1)	29(1)	12(1)	0(1)	0(1)	5(1)
Eu(4)	19(1)	18(1)	13(1)	− 1(1)	− 1(1)	1(1)
Eu(5)	18(1)	23(1)	25(1)	− 8(1)	2(1)	− 4(1)
Eu(6)	18(1)	26(1)	34(1)	− 13(1)	− 4(1)	1(1)

TABLE 4
Coordination Distances (Å) to Each Atom in the Asymmetric Unit in $A_{16}Pn_{11}$

	[a]$Ca_{16}Sb_{11}$	$Eu_{16}Sb_{11}$	$Eu_{16}Bi_{11}$
Pn(1)–*A*(5) (× 2)	3.418(2)	3.527(2)	3.615(3)
Pn(1)–*A*(5) (× 2)	3.867(2)	3.965(2)	3.889(3)
Pn(1)–*A*(6) (× 2)	3.159(3)	3.292(2)	3.480(3)
Pn(1)–*A*(6) (× 2)	3.581(3)	3.708(2)	3.746(4)
Pn(2)–*A*(4) (× 2)	3.240(2)	3.334(2)	3.413(2)
Pn(2)–*A*(4) (× 2)	3.252(2)	3.352(2)	3.423(2)
Pn(2)–*A*(5) (× 2)	3.147(2)	3.282(1)	3.330(3)
Pn(2)–*A*(6) (× 2)	3.232(2)	3.357(2)	3.366(2)
Pn(3)–*A*(1)	3.787(3)	3.967(3)	4.147(2)
Pn(3)–*A*(2)	4.779(3)	4.790(3)	4.666(3)
Pn(3)–*A*(3)	4.193(3)	4.332(3)	4.400(3)
Pn(3)–*A*(3) (× 2)	3.168(2)	3.280(1)	3.337(2)
Pn(3)–*A*(5) (× 2)	3.072(2)	3.211(2)	3.264(3)
Pn(3)–*A*(6) (× 2)	3.131(2)	3.258(2)	3.299(3)
Pn(4)–*A*(1)	3.252(2)	3.339(2)	3.411(4)
Pn(4)–*A*(2)	3.177(2)	3.323(2)	3.399(4)
Pn(4)–*A*(4) (× 2)	3.380(2)	3.492(2)	3.544(2)
Pn(4)–*A*(4) (× 2)	3.397(2)	3.516(1)	3.557(2)
Pn(4)–*A*(5) (× 2)	3.509(2)	3.687(2)	3.904(3)
Pn(4)–*A*(6) (× 2)	4.444(3)	4.553(3)	4.439(3)
Pn(5)–*A*(1)	3.117(1)	3.236(2)	3.266(2)
Pn(5)–*A*(3)	3.071(3)	3.174(2)	3.221(4)
Pn(5)–*A*(4) (× 2)	3.249(2)	3.322(2)	3.371(3)
Pn(5)–*A*(5) (× 2)	3.287(2)	3.569(1)	3.617(2)
Pn(5)–*A*(6) (× 2)	3.423(2)	3.313(2)	3.379(3)
Pn(6)–*A*(2)	3.043(2)	3.169(2)	3.229(2)
Pn(6)–*A*(3)	3.043(3)	3.151(2)	3.203(4)
Pn(6)–*A*(4) (× 2)	3.249(2)	3.344(2)	3.390(4)
Pn(6)–*A*(5) (× 2)	3.287(2)	3.368(2)	3.410(3)
Pn(6)–*A*(6) (× 2)	3.423(2)	3.539(1)	3.590(3)
A(1)–*Pn*(3) (× 2)	3.787(3)	3.967(2)	4.147(3)
A(1)–*Pn*(4) (× 2)	3.252(2)	3.339(2)	3.411(4)
A(1)–*Pn*(5) (× 2)	3.117(6)	3.236(2)	3.266(2)
A(2)–*Pn*(3) (× 2)	4.779(3)	4.790(3)	4.666(3)
A(2)–*Pn*(4) (× 2)	3.177(2)	3.323(2)	3.400(4)
A(2)–*Pn*(6) (× 2)	3.043(2)	3.169(2)	3.229(2)
A(3)–*Pn*(1) (× 2)	4.807(2)	4.956(3)	5.017(3)
A(3)–*Pn*(3) (× 2)	3.168(2)	3.279(1)	3.337(2)
A(3)–*Pn*(3)	4.193(2)	4.332(3)	4.400(2)
A(3)–*Pn*(5)	3.071(3)	3.174(2)	3.221(4)
A(3)–*Pn*(6)	3.043(3)	3.151(2)	3.202(4)
A(4)–*Pn*(2)	3.240(2)	3.333(1)	3.413(2)
A(4)–*Pn*(2)	3.252(2)	3.351(1)	3.422(2)
A(4)–*Pn*(4)	3.380(2)	3.492(2)	3.545(2)
A(4)–*Pn*(4)	3.397(2)	3.515(1)	3.557(2)
A(4)–*Pn*(5)	3.217(2)	3.321(2)	3.371(3)
A(4)–*Pn*(6)	3.043(2)	3.344(2)	3.389(3)
A(5)–*Pn*(1)	3.418(2)	3.527(2)	3.615(3)
A(5)–*Pn*(2)	3.147(2)	3.282(1)	3.331(2)
A(5)–*Pn*(3)	3.072(2)	3.211(2)	3.264(3)
A(5)–*Pn*(4)	3.509(2)	3.687(2)	3.903(3)
A(5)–*Pn*(5)	3.459(2)	3.569(1)	3.617(2)
A(5)–*Pn*(6)	3.287(2)	3.368(2)	3.410(3)
A(6)–*Pn*(1)	3.159(3)	3.292(2)	3.482(6)
A(6)–*Pn*(1)	3.867(2)	3.708(2)	3.743(6)
A(6)–*Pn*(2)	3.232(2)	3.357(2)	3.366(3)
A(6)–*Pn*(3)	3.131(2)	3.259(2)	3.299(3)
A(6)–*Pn*(4)	4.445(2)	4.553(2)	4.439(3)
A(6)–*Pn*(5)	3.203(2)	3.313(2)	3.379(3)
A(6)–*Pn*(6)	3.423(2)	3.539(1)	3.590(3)
A(4)–*A*(4)	3.539(3)	3.614(2)	3.711(3)
[b]*Pn*(1)–*Pn*(2)	0.683(3)	0.666(2)	0.422(7)
Pn(1)–*Pn*(2)	3.614(2)	3.829(2)	3.947(2)
Pn(1)–*Pn*(2)	4.297(2)	4.495(2)	4.360(2)
Pn(2)–*Pn*(2)	3.402(2)	3.396(2)	3.576(3)

[a]E. A. Leon-Escamilla, W.-H. Hurng, E. S. Peterson, and J. D. Corbett, *Inorg. Chem.* **36,** 703 (1997).
[b]Split position, 50% occupancy.

described as consisting of columns of pairs of face-sharing square antiprisms that are joined by means of a square prism to form a columnar chain composed of Eu^{2+} cations and centered by Sb anions. Figure 1 shows the connectivity of the columns of Eu. The columns can be visualized as being built up from prism/$(antiprism)_2$ slabs that are formed by Sb(1), Sb(2), Eu(4), Eu(5), and Eu(6) as shown in Fig. 2.

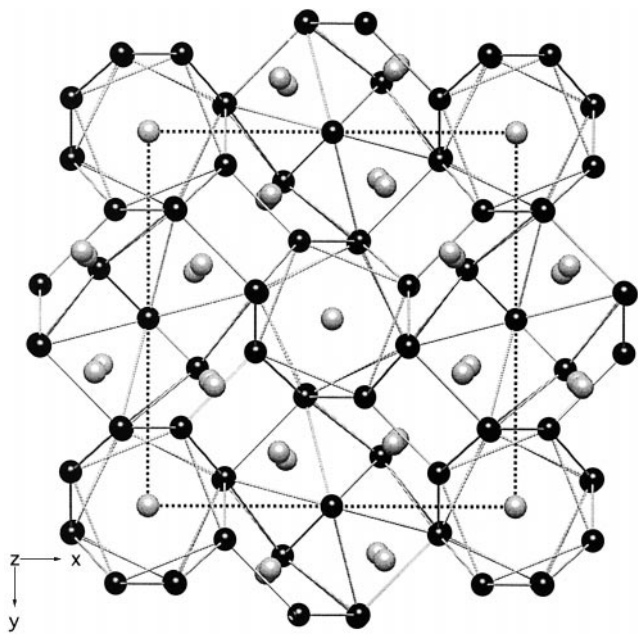

FIG. 1. This figure shows the connectivity of Eu atoms in $Eu_{16}Sb_{11}$. The black and the gray circles represent Eu and Sb, respectively.

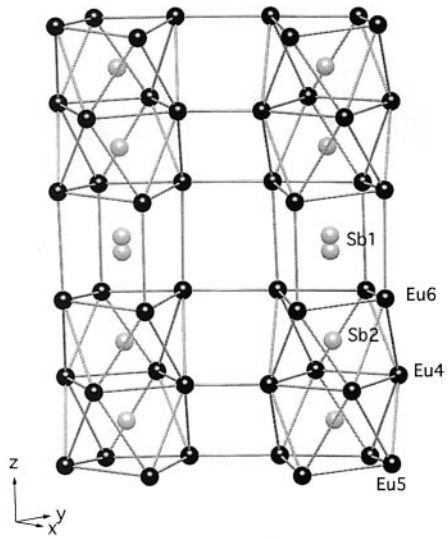

FIG. 2. This illustrates the prism/antiprism slabs that are formed by Sb(1), Sb(2), Eu(4), Eu(5), and Eu(6). The Sb(1) is modeled as a split position, 50% occupancy required by symmetry. Both sites are shown in this figure. The rather short Eu–Eu distances connect the parallel slabs, the shortest being 3.614 Å between Eu(4)'s. The slabs propagate along c as the {prism–antiprism–antiprism} repeats, which gives rise to the shortest Sb–Sb contact in the structure of 3.396 Å between Sb(2)'s.

Sb(1) atoms are located in interstitial sites of the square antiprism surrounded by 8 Eu atoms. Sb(1) is best modeled as a 50 : 50 split site, apparently resulting from the size of the Eu polyhedron. The average distance from the center of the polyhedron is 3.7 Å, 10% larger than that for all other polyhedra in the structure. The columns are made up of Eu–Eu interactions ranging from 3.891(1) to 4.315(1) Å and 3.978(3) to 4.268(3) Å in $Eu_{16}Sb_{11}$ and $Eu_{16}Bi_{11}$, respectively. The Eu–Eu bonds that connect the two parallel columns range from 3.614(2) Å for Eu(4)–Eu(4) to 4.082(1) Å for Eu(6)–Eu(6) in $Eu_{16}Sb_{11}$. The Eu–Eu distances for $Eu_{16}Bi_{11}$ are slightly longer, ranging from 3.711(3) to 4.090(5) Å for Eu(4)–Eu(4) and Eu(6)–Eu(6), respectively. These connections can be idealized as ladder-like along the c axis. Within the cavity formed by the connecting columns, deformed polyhedra of Eu(1) and Eu(2) atoms surround the *Pn* atoms. These pentagonal prisms are also observed in the R_3Rh_2 (R = Gd, Tb, Dy, Ho, Er, Y) phase (18). Examining the coordination around the *Pn*(3) atom in this phase, one finds that the number of neighbors is 9 and the corresponding polyhedra can be described as tricapped-trigonal prism of Eu atoms, with each lateral face capped by another atom similar to the environment in the CaSn, Ca_2Sn, and $Ca_{31}Sn_{20}$ phases (19). Similar also to the R_3Rh_2 phase (18), a ten-coordinated polyhedron for *Pn*(4) is observed for $Eu_{16}Pn_{11}$ with a deformed pentagon. The Eu polyhedron surrounding *Pn*(5) and *Pn*(6) is coordinated with 8 nearest Eu atoms (bicapped-trigonal prismatic) with two faces capped by another Eu(1).

The Eu–*Pn* distances range from 3.152(2) to 3.708(2) Å and 3.203(4) to 3.743(6) Å in $Eu_{16}Sb_{11}$ and $Eu_{16}Bi_{11}$, respectively. The larger Eu–*Pn* distances in Bi can be attributed to the larger Bi ions in the center of the polyhedra making up the columns. The distances are comparable to those reported for $LnM_{1-x}Sb_2$ (Ln = La–Nd, Sm, Gd, Tb; M = Mn, Co, Au, Zn, Cd) where the Ln atom is surrounded by eight antimony atoms with four equivalent Sb distances of 3.256 Å and four other Sb atoms with distances of 3.399 Å (20). The distances are also similar to those found in the $Eu_{11}Sb_{10}$ phase (5), where the Eu–Sb distances range from 3.097 to 3.655 Å and the $Eu_{14}MSb_{11}$ (M = In, Mn) phases where the Eu–Sb distances range from 3.226(1) to 3.894(1) Å (6). The Eu–Bi distances are comparable to the $Eu_{14}MnBi_{11}$ compound (6), which range from 3.318(1) to 3.914(2) Å and 3.334(1) to 3.789(1) Å for the Eu_4Bi_3 compound (3).

The only close *Pn*–*Pn* distances involve *Pn*(1) and *Pn*(2). All other distances are longer than 4.5 Å. Figure 2 shows the antimony Sb(1) and Sb(2) atoms, which repeat as Sb(2′)–Sb(2) ⋯ Sb(1) (or Sb(1′) ⋯ Sb(2″)–Sb(2‴), according to the disorder model) with Sb(2)–Sb(2′) distance of 3.396(2) Å and Sb(2)–Sb(1) distance of 3.829(2) in $Eu_{16}Sb_{11}$. There is a corresponding arrangement in the Bi compound; Bi(2)–Bi(2′) is 3.576(3) Å and Bi(1)–Bi(2) is 3.943(2) Å. The Sb(2)–Sb(2′) distances are longer than the average bonding Sb–Sb distances in solid state compounds where Sb–Sb distances range from 2.8 to 3.0 Å (21, 22). Examples of typical Sb–Sb bonding distances are seen in elementary antimony, 2.91 Å (23, 24), $EuSb_2$ (2.92 Å) (25), NaSb (2.85 and 2.86 Å) (26), and $Eu_{11}Sb_{10}$ (3.037 Å) (5). The Sb–Sb distance of 3.396 Å in the $Eu_{16}Sb_{11}$ phase is only slightly longer than that observed in the $Ba_7Ga_4Sb_9$ phase, where the longest Sb–Sb distance is 3.36 Å (27). The Bi–Bi distances are also quite long compared with that of the average Bi–Bi single bonds. Elemental bismuth has three distances at 3.10 Å and three at 3.47 Å (24). Theoretical calculations on the $Ba_7Ga_4Sb_9$ phase revealed localized bonding and a half-filled Sb–Sb σ^* band (28). In all cases of U_{33} for *Pn*(2) is 2 to 4 times larger than the U_{11}'s (9). The size of Sb(2) U_{33} compared with the other U_{ii}'s in $Ca_{16}Sb_{11}$ was interpreted by Leon-Escamilla *et al.*, as the result of a static displacement that gives rise to an Sb–Sb interaction along the c axis in $Ca_{16}Sb_{11}$. Two possible models have been proposed for the bonding in this phase (9). If Sb_2 is bonded as $[(Ca^{2+})_{16}(Sb^{3-})_9(Sb_2^{4-})e^-]$, this phase is electron rich and expected to be metallic. If Sb–Sb has fractional bonding as $[(Ca^{2+})_{16}(Sb^{3-})_{10}(Sb_2^{4-})_{0.5}]$, proposed to be statistically disordered throughout the structure, then it should be semiconducting. In this disorder model Sb(1) is not bonded to another Sb and is formally 3 − ; Sb(2) is either bonded to another Sb(2′) (total formal charge 4 −) or it is isolated and formally 3 − , therefore providing $1.0Sb^{3+} + 0.5(Sb_2^{4-})$ and the formula is provided above. An alternate interpretation that is consistent with the structure is $[(Ca^{2+})_{16}$

$(Sb^{3-})_8(Sb_3^{8-})$]. This formula notation emphasizes the Pn_3 units that are loosely associated down the z axis. Note that the splitting of the $Pn(1)$ site provides a disorder model; the refined $Pn(2)$ is a composite of two structurally different atoms, one that is terminal and one that is central in the Pn_3^{8-} unit. This model is basically equivalent to that proposed by Leon-Escamilla *et al.*, except that we have not speculated on how the electrons are distributed within the Pn_3^{8-} unit. Electronic calculations would provide insight into the structure and bonding of this compound.

The room temperature resistivity of a pressed pellet of $Ca_{16}Sb_{11}$ shows insulating (or semiconducting) behavior (resistivity is 3×10^5 Ω-cm at room temperature) (9). Figure 3 shows the normalized resistivity for $Eu_{16}Sb_{11}$ as a function of temperature and the inset shows that $\ln(\rho/\rho_{300})$ versus inverse temperature is linear over the temperature range 150–300 K. It is a semiconductor with a room temperature resistance of approximately 3×10^3 Ω-cm. Although this is not quite as large a value as that reported for $Ca_{16}Sb_{11}$, $Eu_{16}Sb_{11}$ clearly is a semiconductor.

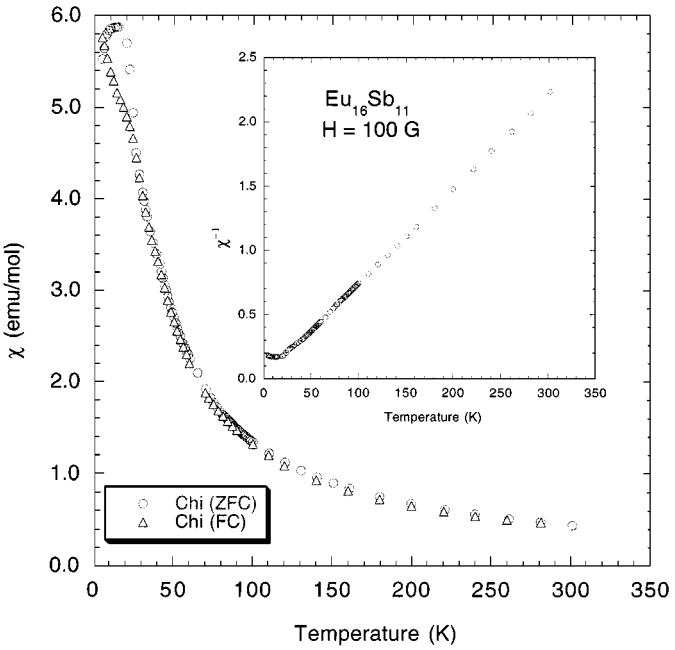

FIG. 4. Temperature-dependent magnetic susceptibility and reciprocal susceptibility for $Eu_{16}Sb_{11}$ at 100 Oe.

Magnetic Properties. Figure 4 shows the magnetic susceptibility and the inverse susceptibility as functions of the temperature (T) for $Eu_{16}Sb_{11}$ at 100 Oe. Analysis of the data shows that the high-temperature susceptibility of each of these compounds follows a modified Curie–Weiss law ($\chi = \chi_0 + \chi/(T - \Theta)$) with an effective moment (determined by the Curie constant, C, provided in Table 5) of $\mu_{exp} = 32.2$ (1) μ_B per formula unit (8.06(3) μ_B/Eu), which is in good agreement for 16 Eu^{2+} ions ($\mu_{eff} = 31.6\ \mu_B$). The Θ obtained from the fit of the data to the modified Curie–Weiss law is nearly zero, and there is no sign of a phase transition in the FC (field-cooled) susceptibility, yet there is a discontinuity in the ZFC (zero-field-cooled) susceptibility at about 15 K, suggesting a possible spin glass state at low temperature. The magnetization at $T = 5$ K is approximately

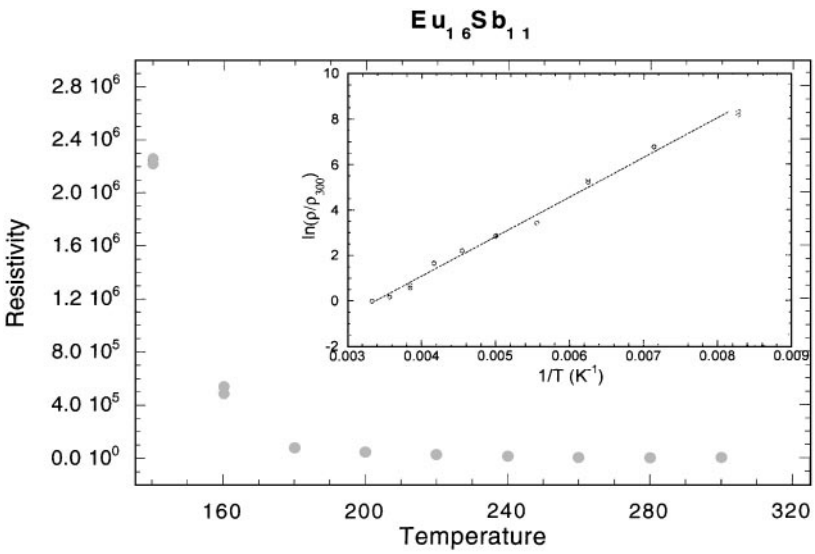

FIG. 3. Temperature-dependent normalized resistivity of $Eu_{16}Sb_{11}$. The inset shows the $\ln(\rho/\rho_{300})$ vs inverse temperature.

TABLE 5
Magnetic Properties of $Eu_{16}Sb_{11}$ and $Eu_{16}Bi_{11}$

	$Eu_{16}Sb_{11}$	$Eu_{16}Bi_{11}$
χ_0[a] (emu/mol)	0.019(7)	− 0.002(7)
C[a] (emu K/mol)	130(1)	141(2)
Θ[a] (K)	1.3(3)	− 12(1)
μ_{exp}[b] (μ_B/f.u.)	32.2(1)	33.6(2)
μ_{exp}(μ_B/Eu)	8.06(3)	8.40(6)

[a]Obtained from fitting the data to equation $\chi = \chi_o + C/(T - \Theta)$.
[b]Using the equation $\mu_{exp} = (7.99C)^{1/2}$.

linear, and there is no measureable hysteresis (Fig. 5). The magnetic properties of $Eu_{16}Sb_{11}$ are similar to those of $Eu_{14}InSb_{11}$ (6) and Eu_4Bi_3 (3), where a transition temperature near 15 K is observed.

Figure 6 shows the temperature-dependent magnetic susceptibility and the inverse susceptibility of $Eu_{16}Bi_{11}$ measured at 1000 Oe. The Θ obtained for the fit of the data to the Curie–Weiss law is − 12, consistent with antiferromagnetic ordering, and there is no sign of a phase transition in the FC susceptibility with $\mu_{exp} = 33.6$ (2) μ_B/f.u.. However, there is a change in slope at low temperatures. Figure 7 shows the field-dependent magnetic susceptibility for $Eu_{16}Bi_{11}$. Although a small hysteresis is observed at low field, the magnetization is nearly linear and no saturation is observed. This effect is unusual and none of the related phases show similar hysteresis, but suggests that there may be some canting of spins at low field. More detailed studies of ac susceptibility would provide insight into this low-field phenomena.

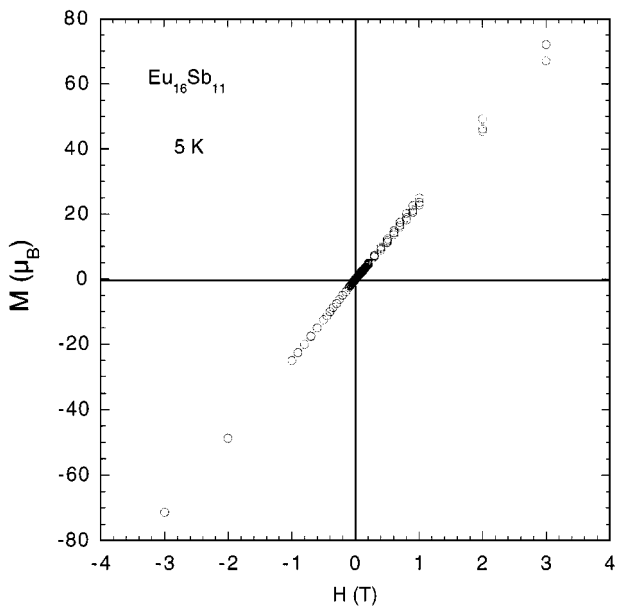

FIG. 5. Field-dependent magnetic moment for $Eu_{16}Sb_{11}$ at 5 K.

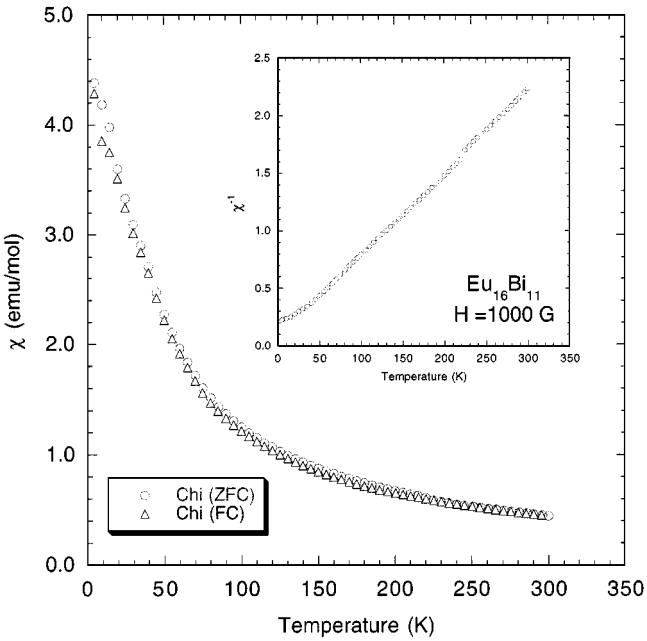

FIG. 6. Temperature-dependent magnetic susceptibility and reciprocal susceptibility for $Eu_{16}Bi_{11}$ at 1000 Oe.

SUMMARY

The $Eu_{16}Pn_{11}$ phases are isostructural to the reported complex Zintl-phase $Ca_{16}Sb_{11}$. The magnetic data are consistent with all the Eu atoms being Eu^{2+} cations. The resistivity show semiconducting behavior. The magnetic and electronic data are most consistent with the static disorder model suggested previously (9) with all the electrons localized. The $Eu_{16}Pn_{11}$ phases presented here have some of the characteristics desired for thermoelectric materials. Most recently, research on new thermoelectrics has aimed toward binary and ternary covalently bonded semiconductors, especially with "rattling" atoms or molecules (29). The properties desired include high Seebeck coefficient (insulating) materials and a large electronic contribution to thermal conductivity. The cagelike structure, high coordination, large atomic mass, and weakly bound atom in the "cage" of the $A_{16}Pn_{11}$ phase are some of the characteristics that make these possible candidates for thermoelectric materials. In addition, the implications of the structural model suggest that possible ferroelectric or piezoelectric properties are worth investigating. The results of the present investigation warrant further property measurements and theoretical calculations.

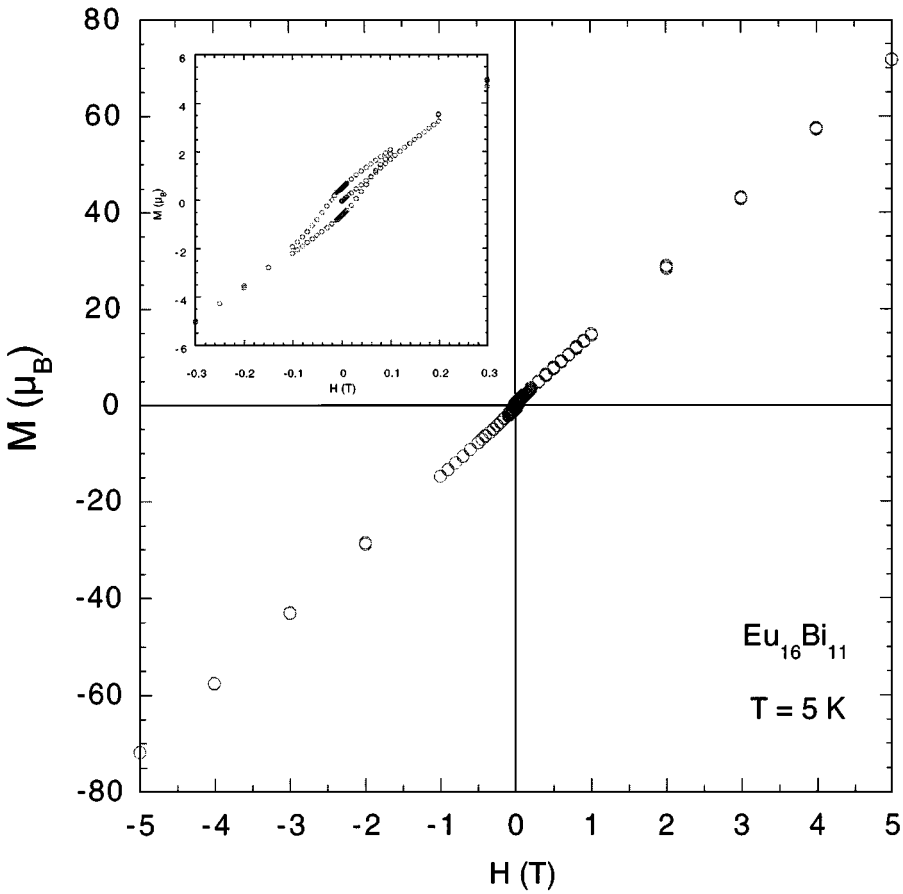

FIG. 7. Field-dependent magnetic moment for $Eu_{16}Bi_{11}$ at 5 K. The inset shows an expanded view of the hysteresis plot.

ACKNOWLEDGMENTS

We thank P. Klavins for assistance and R. N. Shelton for use of the magnetometer. We thank Tadashi C. Ozawa and Sean McWhorter for collecting the temperature-dependent resistivity data. Financial support by the National Science Foundation, Division of Materials Research (DMR-9505565, 9803074) is gratefully acknowledged.

REFERENCES

1. K. A. Gschneidner, Jr., and L. Erying, "Handbook of the Physics and Chemistry of Rare Earths." Elsevier, New York, 1979.
2. G. D. Brunton and H. Steinfink, *Inorg. Chem.* **10,** 2301 (1971).
3. M. E. Wang, J. T. Chang, and S. M. Kauzlarich, *Z. Anorg. Allg. Chem.* **622,** 432 (1996).
4. H. L. Clark, H. D. Simpson, and H. Steinfink, *Inorg. Chem.* **9,** 1962 (1970).
5. R. Schmelczer, D. Schwarzenbach, and F. Hulliger, *Z. Naturforsch B* **36,** 1213 (1979).
6. J. Y. Chan, A. Rehr, D. J. Webb, and S. M. Kauzlarich, *Chem. Mater.* **9,** 2131 (1997).
7. S. Methfessel and E. Kneller, *Appl. Phys Lett.* **2,** 115 (1963).
8. F. Hulliger, *in* "Handbook on the Physics and Chemistry of Rare Earths" (K. A. Gschneidner and L. Eyring, Eds.). Vol. 4, p. 153, Elsevier, North-Holland, New York, 1979.
9. E. A. Leon-Escamilla, W.-M. Hurng, E. S. Peterson, and J. D. Corbett, *Inorg. Chem.* **36,** 703 (1997).
10. G. S. Smith, Q. Johnson, and A. G. Tharp, *Acta Crystallogr.* **23,** 640 (1967).
11. M. Marinez-Ripoll and G. Brauer, *Acta Crystallogr. B* **30,** 1083 (1974).
12. C. M. Clark, D. K. Smith, and G. J. Johnson, "POWDER." Department of Geosciences, Pennsylvania State University, University Park, PA, 1973.
13. H. Imoto, "GUIN." Iowa State University, 1979.
14. K. Lii, S. Wang, and E. Garcia, "LATT," Iowa State University, 1985.
15. S. Parkin, B. Moezzi, and H. Hope, *J. Appl. Crystallogr.* **28,** 53 (1995).
16. G. M. Sheldrick, "SHELXL97." University of Göttingen, Germany, 1997.
17. Quantum Design Inc., San Diego, CA, 92121.
18. J. M. Moreau, D. Paccard, and E. Parthé, *Acta Crystallogr. B* **32,** 1767 (1976).
19. M. L. Fornasini and E. Franceschi, *Acta Crystallogr. B* **33,** 3476 (1977).
20. P. Wollesen, W. Jeitschko, M. Brylak, and L. Dietrich, *J. Alloys Compd.* **245,** L5 (1996).
21. B. Eisenmann, *Z. Naturforsch. B* **34,** 1162 (1979).

22. E. Brechtel, G. Cordier, and H. Z. Schäfer, *Z. Naturforsch B* **36,** 1341 (1981).
23. C. S. Barrett, P. Cucka, and K. Haefner, *Acta Crystallogr.* **16,** 451 (1963).
24. A. F. Wells, "Structural Inorganic Chemistry, 1-701." Oxford Univ. Press, New York, 1975.
25. F. Hulliger and R. Schmelczer, *J. Solid State Chem.* **26,** 389 (1978).
26. D. T. Cromer, *Acta Crystallogr.* **12,** 41 (1959).
27. G. Cordier, H. Schäfer, and M. Stetler, *Z. Anorg. Allg. Chem.* **534,** 137 (1986).
28. P. Alemany, S. Alvarez, and R. Hoffmann, *Inorg. Chem.* **29,** 3070 (1990).
29. G. Mahan, B. Sales, and J. Sharp, *Phys. Today* **50,** 42 (1997).